

# Blunt notch effect on the fatigue response up to $10^9$ cycles of selective laser melting Ti6Al4V specimens

Andrea Tridello<sup>1</sup>  | Carlo Boursier Niutta<sup>1</sup>  | Filippo Berto<sup>2</sup>  |  
Davide S. Paolino<sup>1</sup> 

<sup>1</sup>Department of Mechanical and Aerospace Engineering, Politecnico di Torino, Turin, Italy

<sup>2</sup>Department of Chemical Engineering, Materials and Environment, Università La Sapienza, Rome, Italy

## Correspondence

Andrea Tridello, Department of Mechanical and Aerospace Engineering, Politecnico di Torino, Turin 10129, Italy.  
Email: [andrea.tridello@polito.it](mailto:andrea.tridello@polito.it)

## Abstract

In this paper, the influence of a blunt notch on the VHCF response of SLM Ti6Al4V specimens is investigated. Ultrasonic fully reversed tension–compression tests up to  $10^9$  cycles were carried out on unnotched specimens and specimens with a blunt notch. Unnotched specimens show a slightly larger fatigue response, with limited differences. All fatigue failures originated from defects, which are bigger in unnotched specimens, mainly due to the different risk volume of the tested specimens and the related size effect. Interactions between notch, stress gradient, and defect size distribution must be considered to properly assess the influence of notch on the VHCF response.

## KEYWORDS

additive manufacturing (AM), selective laser melting (SLM), size effect, Ti6Al4V, very high cycle fatigue (VHCF)

## Highlights

1. The influence of a blunt notch on the VHCF response of SLM Ti6Al4V alloy is investigated.
2. The feasibility of ultrasonic VHCF tests on SLM Ti6Al4V specimens is proved.
3. Surface defects play a major role even in SLM specimens with blunt notches.
4. Defects and related size effect can limit the stress concentration effect.

## 1 | INTRODUCTION

In the last years, the use of components produced by Additive Manufacturing (AM) processes has tremendously increased in several industrial sectors, like the aerospace and biomedical sectors.<sup>1,2</sup> AM processes allow to manufacture components with unprecedented complex shapes and

geometrical features, tailored and customized to the final application, which cannot be produced with traditional manufacturing technologies, like subtractive technologies. Topology optimization (TO in the following) algorithms can be effectively exploited for the design of components to be produced with AM processes. TO provides the optimized material distribution capable to withstand the

This is an open access article under the terms of the [Creative Commons Attribution-NonCommercial-NoDerivs](https://creativecommons.org/licenses/by-nc-nd/4.0/) License, which permits use and distribution in any medium, provided the original work is properly cited, the use is non-commercial and no modifications or adaptations are made.

© 2023 The Authors. *Fatigue & Fracture of Engineering Materials & Structures* published by John Wiley & Sons Ltd.

applied loads, through an iterative process based on finite element analyses (FEAs).<sup>3</sup> With TO and AM, the component performance can be enhanced and its weight can be reduced, without affecting its structural integrity. Due to this design freedom and the limited manufacturing constraints of AM processes, notches with different degrees of severity can be present in the final geometry. Notches strongly influence the structural integrity of components and their effect on the mechanical response must be properly accounted for, especially if fatigue loads are applied.

The influence of notches on the fatigue response of AM components, which is generally driven by defects,<sup>4,5</sup> up to the high cycle fatigue (HCF) life range has been quite extensively investigated in the recent and past literature, even if there are still several unsolved and challenging open questions as those concerning the mechanisms of crack initiation and the interactions between the region with stress concentration and manufacturing defects. In Solberg et al.,<sup>6</sup> notch effect on the fatigue response of as-built and heat-treated Inconel 718 specimens is investigated. Significant notch effects have been found by testing unnotched and V-notched specimens. The S–N curves have been assessed with the Murakami model,<sup>7</sup> highlighting the influence of defects on the crack nucleation process. In Solberg and Berto,<sup>8</sup> experimental tests have been carried out on specimens with semicircular and V-shaped notches. All the specimens failed from defects placed close to the surface region. A notch sensitivity between zero and one for V-notch shape and above one for semicircular notch was experimentally found, explainable with the low quality of the downward surface and suggesting that the notch sensitivity is a “material-component” parameter, rather than a “material parameter.” In Solberg and Berto,<sup>9</sup> the authors have highlighted the need of modelling the interactions between defects and geometrical features and proposed a diagram for the prediction of failure locations in Inconel 718 notched specimens produced through AM. Similarly, in Molaei et al.,<sup>10</sup> methodologies commonly used for assessing the notch severity in traditionally built materials have been compared. The critical plane-based method and fracture mechanics approaches have been used for analyzing the correlation between fatigue data obtained through uniaxial and multiaxial data, showing that both approaches can satisfactorily fit the experimental results. In Emanuelli et al.,<sup>11</sup> the influence of notch and posttreatments on the fatigue response of an SLM Ti6Al4V alloy has been investigated. Compressive residual stresses induced by posttreatments can shift crack initiation below the surface. On the other hand, the crack can nucleate on the specimen surface after heat treatments, being this effect more evident in notched specimens characterized by a peak stress in the small region close to the notch tip. The authors have also highlighted

the interaction between defects and notches and the importance of assessing the critical volume close to the notch region.

According to the above literature analysis, notch effect on the fatigue response of AM components is a very complex phenomenon, with defects playing a significant role and interacting with the material volume subjected to high-stress values close to the notch tip. More efforts and more research are necessary to understand these mechanisms and to ensure a safe design of AM components with complex geometries. Moreover, to the best of the authors' knowledge, no experimental results or research on the influence of notch on the very high cycle fatigue (VHCF) response of AM parts are available at present. However, the assessment of the fatigue response of AM parts even in the VHCF region is of utmost importance due to the increased required durability of components.<sup>12–16</sup>

In the present paper, notch effect on the VHCF response of AM specimens has been experimentally investigated. Ultrasonic fully reversed tension–compression tests have been carried out up to  $10^9$  cycles on notched and unnotched specimens. In the first part, the definition of stress concentration factor for specimens subjected to ultrasonic fatigue tests<sup>17</sup> is recalled and discussed. Specimens with blunt notches for ultrasonic fatigue tests have been designed, by comparing specimen shapes commonly tested in the VHCF literature. Thereafter, the stress amplitude at the specimen center assessed with finite element analyses (FEAs) has been validated with strain gages. Finally, experimental tests on notched and unnotched specimens have been carried out and the influence of defects and notch has been investigated.

The present research aims at filling the gap of knowledge regarding the notch effect on the VHCF response of AM materials. According to the above literature analysis, at present, no results are available on notch effect on the VHCF response of AM specimens. In general, results on notch effect on the VHCF response are quite limited,<sup>18–22</sup> due to the complexity of designing specimens with notches for ultrasonic fatigue tests. In the paper, a straightforward procedure is defined, by comparing the specimen geometries generally subjected to ultrasonic fatigue tests and by analyzing a stress concentration factor, the dynamic stress concentration factor, specifically defined for specimens subjected to ultrasonic fatigue tests.<sup>17</sup> Moreover, the literature results on notch effect on the fatigue response of AM specimens, besides being limited to the LCF–HCF life range despite the importance of the VHCF life region, are contradictory. The results obtained in the present work through ultrasonic fatigue tests up to the VHCF life region can be generalized and extended to the other fatigue life regions, since they point out the strong interactions between local stress concentration, loaded volume, and

defects and thus contribute to improve the knowledge on notch effect on the fatigue response of AM specimens, fundamental to guarantee their structural integrity.

## 2 | SPECIMEN DESIGN AND EXPERIMENTAL ACTIVITY

In this section, the experimental activity is described in detail. In Section 2.1, the definition of stress concentration factor for specimens subjected to ultrasonic fatigue tests in Paolino et al.<sup>17</sup> is recalled and discussed. In Section 2.2, the procedure followed for the design of specimens with blunt notch is described. Section 2.3 deals with the material and the AM process for the specimen production. Finally, in Section 2.4, the testing configuration and the strain gage calibration are described.

### 2.1 | Dynamic stress concentration factor

In conventional tension–compression or rotating bending fatigue tests, the stress concentration factor associated to the tested specimens ( $k_t = \frac{s_{max}}{s_{nom}}$ , being  $s_{max}$  the maximum stress and  $s_{nom}$  the nominal stress) can be reliably assessed through available charts<sup>23</sup> or finite element analysis (FEA). On the other hand, a definition of a stress concentration factor for specimens subjected to ultrasonic fatigue tests is not available. Indeed, the stress distribution in specimens subjected to ultrasonic fatigue tests is given by the stress wave propagation within the specimen<sup>13</sup> and the specimens are designed to have the first longitudinal mode of vibration close to 20 kHz. Accordingly, the stress amplitude is not computed by considering the applied load and the cross-sectional area, and the nominal stress cannot be assessed, since the stress amplitude varies even in the specimen part with a constant cross-section. In Akiniwa et al.,<sup>18</sup> ultrasonic fatigue tests are carried out on specimens with different notches. The notch severity associated to each specimen is assessed by comparing the  $k_t$  values. In the following, the definition of stress concentration factor for specimens subjected to ultrasonic fatigue tests,  $k_{t,d}$ , provided in Paolino et al.<sup>17</sup> is considered:

$$k_{t,d} = \frac{s_{max}}{s_{long, max}}, \quad (1)$$

being  $s_{max}$  the maximum stress amplitude and  $s_{long, max}$  the maximum stress on the specimen longitudinal axis.  $s_{max}$  and  $s_{long, max}$  can be reliably computed with FEA.  $s_{long, max}$  can be therefore considered as the nominal stress in specimens subjected to ultrasonic fatigue tests. With the  $k_{t,d}$  definition, the severity of notches in specimens subjected to ultrasonic fatigue tests can be reliably assessed and compared.

### 2.2 | Specimens with blunt notch: Design methodology

In this section, the methodology followed for the design of specimens with blunt notches is described. Among the specimen shapes used for ultrasonic fatigue tests, two specimen geometries available in the literature have been considered. The first one is the typical hourglass geometry.<sup>13</sup> The second one is the Gaussian specimen shape, proposed by the research group of the Politecnico di Torino.<sup>17</sup> This shape has been considered since it ensures an almost uniform stress distribution along the gage length. Figure 1A,B shows the hourglass and the Gaussian specimen shapes, respectively, modified in order to induce a stress concentration with a blunt notch. The parameters  $D_h$ ,  $r_c$ ,  $d$ , and  $D_l$ , highlighted in red, are those that have been varied to design a specimen with a ratio between the largest and the smallest diameter equal to 3 ( $\frac{D_h}{d} = 3$ ) and a ratio between the radius  $r_c$  and  $d$  equal to 1 ( $\frac{r_c}{d} = 1$ ). With this geometry, the influence of blunt notches on the VHCF response can be reliably tested with the available ultrasonic testing machines. The other parameters (in blue in the figure),  $L$  for the hourglass geometry and  $L_h$ ,  $L_1$ , and  $L_g$  for the Gaussian shape, are varied to tune the first longitudinal mode of vibration close to 20 kHz.

For the analysis of the stress concentration, finite element analyses (FEAs) have been carried out with the commercial software Ansys, by considering half of the specimen length and by using axisymmetric plane 82 elements. A modal analysis has been carried out, with the displacement at the specimen center set equal to

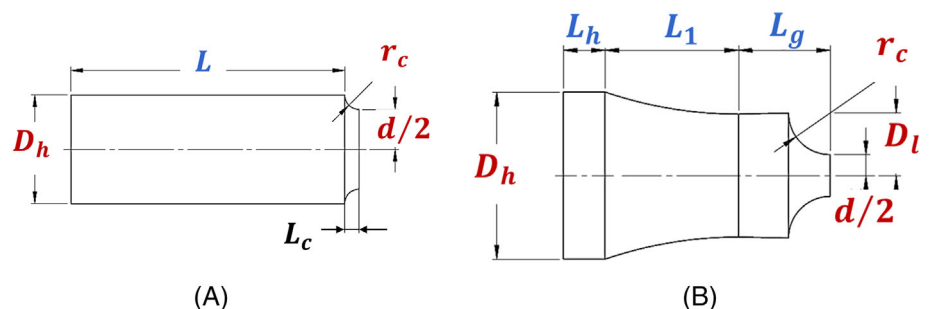


FIGURE 1 Geometries considered for the design of specimens with blunt notches: (A) hourglass geometry and (B) Gaussian geometry. [Colour figure can be viewed at [wileyonlinelibrary.com](https://onlinelibrary.wiley.com)]

TABLE 1 Comparison between the  $k_t$  and  $k_{t,d}$  values for the investigated specimen geometries.

| $r_c$ (mm) | $\frac{r_c}{d}$ | $\frac{D_h}{d}$ | $k_t$ | $k_{t,d}$ (hourglass) | $k_{t,d}$ (Gaussian) |
|------------|-----------------|-----------------|-------|-----------------------|----------------------|
| 5          | 1               | 3               | 1.21  | 1.43                  | 1.43                 |
| 6          | 1               | 3               | 1.21  | 1.43                  | 1.43                 |
| 7          | 1               | 3               | 1.21  | 1.43                  | 1.43                 |

0. The mesh has been refined close to the region where the peak stress occurs, with the element size smaller than 0.25 mm. A mesh convergence has been moreover carried out, with the final configuration ensuring a variation of the dynamic stress concentration factor smaller than 0.6%. The specimen is manufactured with the Ti6Al4V alloy by considering average elastic properties for the Ti6Al4V powders used for the SLM processes, that is, Young modulus of 110 GPa, density of 4428 kg/m<sup>3</sup>, and Poisson ratio of 0.34. The  $r_c$  value has been varied in the range [5 : 7] mm, with steps of 1 mm. Table 1 summarizes the main results of the simulations and compares the  $k_t$  and  $k_{t,d}$  values for the two investigated specimen shapes. The  $k_t$  values have been computed with FEAs.

According to Table 1, the  $k_{t,d}$  values are larger than the static  $k_t$  values. Moreover, the hourglass and the Gaussian geometries provide the same  $k_{t,d}$ , with the stress concentration mainly driven by the ratio between diameters and by the radius  $r_c$ , regardless of the specimen shape. Accordingly, hourglass geometry has been selected (and is to be preferred) since easier to manufacture. Among the three investigated radius  $r_c$ , the solution with  $r_c = 6$  mm has been chosen, since it ensures a larger frequency distance between the longitudinal mode of vibration close to 20 kHz and the torsional and bending modes. This is a fundamental parameter to be considered when specimens for ultrasonic fatigue tests are designed, since it ensures that bending and torsional spurious stresses are not induced during the experimental tests.

Figure 2A shows the final geometry of the specimen with blunt notch with  $k_{t,d}$  equal to 1.428 (“notch specimen” in the following). An hourglass specimen with the same  $d$  and  $\frac{D_h}{d}$  and  $k_{t,d}$  close to 1 has been also designed, according to standard procedures.<sup>13,17</sup> The geometry has been iteratively varied to minimize the  $k_{t,d}$  value. The final geometry of the hourglass specimen providing a  $k_{t,d}$  equal to 1.024 (“unnotched specimen” in the following) is shown in Figure 2B.

Figure 2C shows the stress amplitude along the axial direction ( $s_a$ ) within the specimen with notch, normalized by maximum stress measured on the specimen axis. Figure 2D shows the longitudinal stress amplitude measured on the specimen surface ( $s_{a,surf}$ ), normalized by the maximum stress within the specimen ( $s_{max}$ ) along the axial coordinate,  $y$ , normalized by the length  $L_c$  (Figure 1). The region between  $y=0$ , corresponding to

the specimen center, and  $y=L_c$  is shown, that is, the notch region.

### 2.3 | Experimental material and AM process

Ti6Al4V ELI powder has been used for manufacturing the specimens with a selective laser melting process (SLM). Specimens have been produced by the Beam It group, with standard process parameters optimized for industrial applications. They have been built in vertical direction (i.e., longitudinal axis perpendicular to the building platform), with a layer thickness of 60  $\mu$ m and the building platform heated to 180°C, and thereafter subjected to a stress relief heat treatment, with a heating temperature of 740°C. This heat treatment, commonly used for industrial applications, allows to minimize residual stresses, according to Günther et al.,<sup>24</sup> in which similar heating temperatures and time have been considered. For the specimens with notches, as thin as possible, supporting structures have been designed and optimized by the specimen manufacturers and mechanically removed after the AM process, paying attention not to damage the gage section. Figure 3 clarifies the region (in green) where the support structures have been manufactured. In particular, supporting structures have been manufactured in the small circular region with external diameter equal to  $D_h$ , shown in green in Figure 3, to support the upper horizontal surface (red surface in Figure 3).

It must be noted that the full set of process parameters cannot be disclosed for confidentiality reasons.

Before running the experimental tests, specimens have been manually polished with sandpapers with increasing grit, up to 1000#, to remove macro surface scratches that could cause a premature specimen failure, according to a common practice for ultrasonic fatigue tests.<sup>25–27</sup>

### 2.4 | Ultrasonic fatigue testing setup and stress calibration

Fully reversed tension–compression tests at constant stress amplitude have been carried out by using the ultrasonic testing machines developed at the Politecnico di Torino. The applied stress amplitude has been kept constant through a closed-loop control based on the displacement measured by a laser sensor at the free specimen end. The

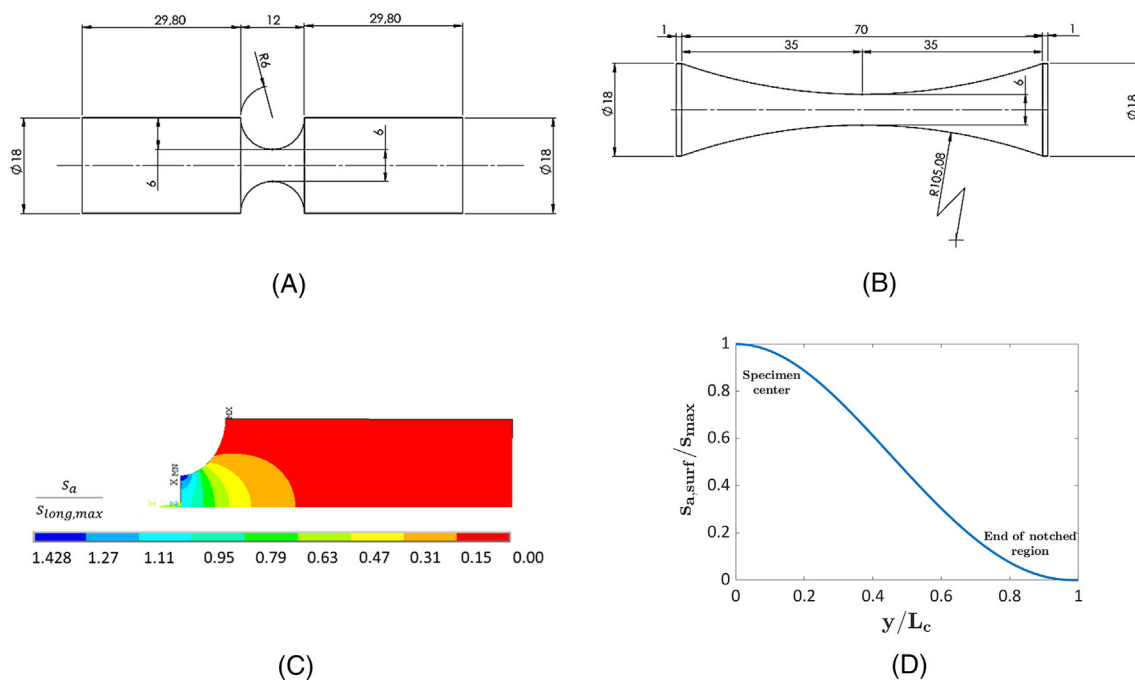


**FIGURE 2** Geometries of the specimens for assessing the blunt notch effect: (A) hourglass specimens with notch (notched specimen) and (B) hourglass specimen without notch (unnotched specimen). (C) Longitudinal stress amplitude distribution in notched specimens and (D) longitudinal stress amplitude measured on the notched specimen surface (normalized by the maximum stress within the specimen) with respect to the axial coordinate (only the notch region is shown). [Colour figure can be viewed at [wileyonlinelibrary.com](http://wileyonlinelibrary.com)]

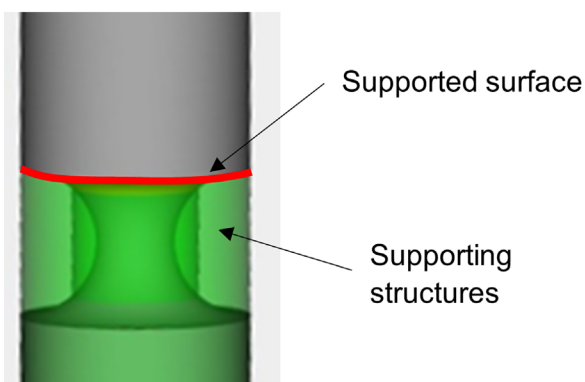


**FIGURE 3** Details of the specimen region where the support structures have been manufactured. [Colour figure can be viewed at [wileyonlinelibrary.com](http://wileyonlinelibrary.com)]

specimen temperature has been monitored in real time with an infrared sensor and kept below 25°C by using two vortex tubes placed near the specimen center. Figure 4 shows the ultrasonic testing setup, with the temperature sensor, the displacement sensors, and the vortex tubes in a typical testing configuration. The specimen is rigidly connected to the horn with an adhesive butt joint. A two-component, cyanoacrylate/acrylic hybrid adhesive, ensuring high strength and fast fixturing time, has been used.

Before beginning the experimental tests, the applied stress amplitude in notched specimens and the corresponding FEA model have been validated with strain

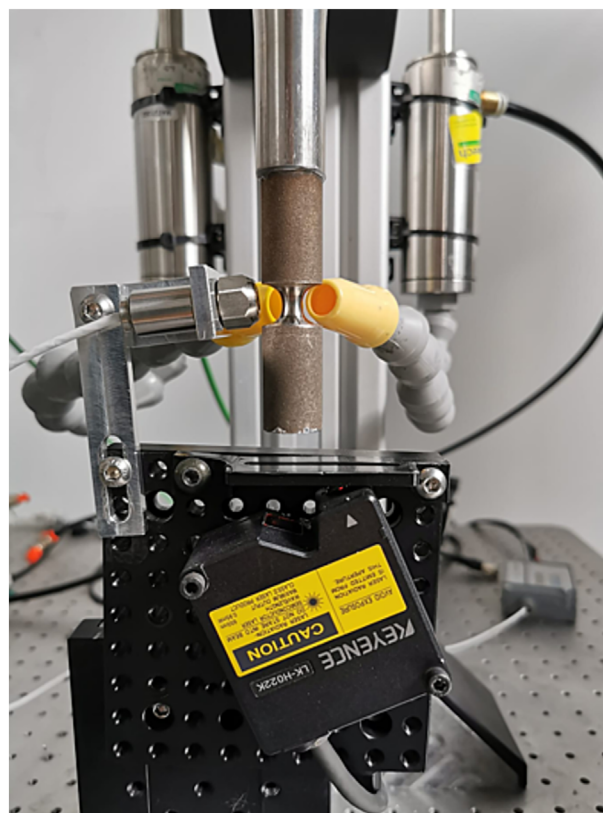


**FIGURE 4** Ultrasonic fatigue testing setup in a typical testing configuration. [Colour figure can be viewed at [wileyonlinelibrary.com](http://wileyonlinelibrary.com)]

gages. A strain gage rosette (HBM 1-XY91-1.5/350, strain gage 1 in the following) in half-bridge configuration has been bonded on the specimen part with constant cross-section (with length  $L$ , according to Figure 1). Within this specimen part, the measuring point with the largest stress amplitude has been selected, to have a high signal-to-noise ratio. Figure 5A shows the specimen with the attached strain gage 1.

A second strain gage calibration has been carried out by using a micro strain gage (HBM 1-LY11-0.3/120, strain gage 2 in the following), with 0.3 mm grid length, bonded as close as possible to the specimen center. Figure 5B shows the specimen with the micro strain gage bonded on the specimen.

For both validations, a high-speed Elsys strain gage acquisition system has been used for the completion of the Wheatstone bridge and to amplify the gage signal. The measuring system has been completed with the National Instrument DAQ NI 6363, acquiring the gage signal at a sample rate of 300 kHz.

### 3 | EXPERIMENTAL RESULTS

In this section, the experimental results are analyzed. In Section 3.1, the results of the strain gage calibration are analyzed. In Section 3.2, the S-N plot of the experimental data is reported; whereas in Section 3.3 the failure origin is investigated with the scanning electron microscope (SEM). Finally, in Section 3.4, the fatigue failure data are analyzed with literature models and compared with literature results.

#### 3.1 | Strain gage calibration: Experimental results

In this section, the results of the strain gage calibration are analyzed in detail. Figure 6A plots the stress

amplitude acquired by strain gage 1 with respect to the displacement exerted by the piezoelectric transducer. In Figure 6A, the green square markers are the experimental data, whereas the blue circular markers are the stress amplitude computed through FEA by considering an initial displacement amplitude computed analytically (i.e., by multiplying the initial displacement exerted by the piezoelectric transducer multiplied by the amplification factors of the booster and the horn). The Young modulus in the datasheet by the specimen manufacturer has been verified through an experimental-numerical procedure after the specimen production. In particular, after the polishing process, the specimen resonance frequency associated with the longitudinal mode of vibration, that is, the one excited during the ultrasonic fatigue tests, has been experimentally measured with the impulse excitation technique.<sup>28</sup> Thereafter, an FE analysis has been carried out to assess the longitudinal resonance frequency, starting from the specimen geometry measured with a high-resolution digital caliber. The dynamic Young modulus in input in the FE model ensuring a match between the experimental and numerical longitudinal resonance frequency has been considered for the subsequent analyses concerning the validation of the stress distribution within the specimen.

Figure 6B shows the result of the calibration with strain gage 2. As before, the green square markers refer to the experimental results, whereas the blue circular markers represent the stress amplitudes computed through FEA and by considering an initial displacement computed analytically. For both calibrations, the experimental stress amplitude has been computed through a harmonic interpolation of the acquired strain gage signal. The FE model described in Section 2 has been used for the computation of the numerical stress amplitude, by considering the exact gage locations measured with a digital caliber (resolution of 0.01 mm). The calibration has been

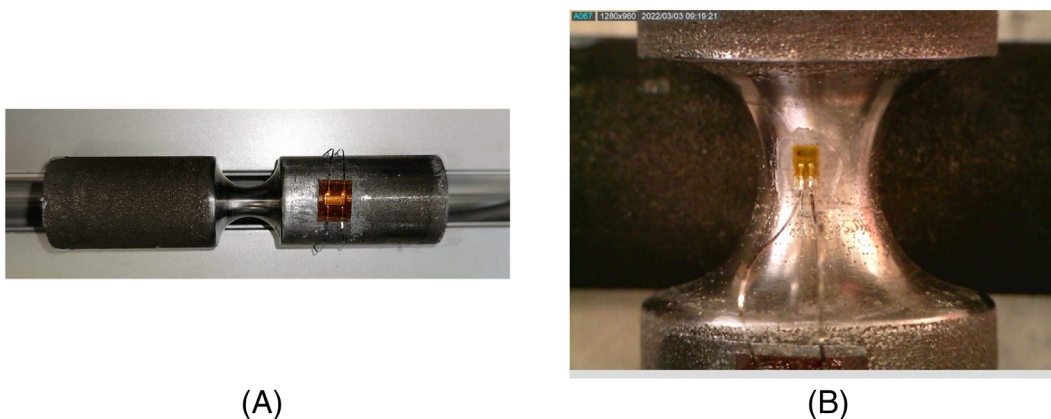


FIGURE 5 Strain gage calibration of notched specimens: (A) strain gage rosette attached in specimen part with length  $L$  (strain gage 1) and (B) micro strain gage attached at the specimen center (strain gage 2). [Colour figure can be viewed at [wileyonlinelibrary.com](http://wileyonlinelibrary.com)]

carried out at small stress amplitude levels, to avoid damaging of the strain gages and the temperature increment.

According to Figures 6A,B, the numerical data are in good agreement with the experimental data, with the FEA and the experimental markers overlapping and following the same linear trend. Accordingly, the stress amplitude at the specimen center can be reliably assessed with the developed FE model. The correlation between the applied displacement amplitude and the stress at the specimen center has been also verified for the unnotched hourglass specimens, according to a procedure commonly adopted in the literature.<sup>27</sup>

### 3.2 | S–N plot of the experimental data

In this section, the experimental results are reported in an S–N plot (Figure 7) and analyzed.

According to Figure 7, unnotched specimen data are above the data points obtained by testing notched specimens, but the difference is not so large, with the data tending to overlap. Unnotched specimen data are above notch data for number of cycles close to  $10^6$ , whereas there is no difference for number of cycles above  $10^7$ . However, a reliable comparison is rather difficult due to the larger scatter of the experimental data,<sup>24</sup> especially for notch specimens. For example, for stress amplitudes below 220 MPa, runout data and failures below  $10^7$  cycles have been concurrently found in notched specimens. The large scatter of AM data can be generally explained by considering that failures are driven by defects randomly distributed within the loaded volume.<sup>4,5,29</sup> Accordingly, the analysis of the experimental results of AM specimen cannot disregard a thorough analysis of the defect population.

### 3.3 | Defect analysis

All the fracture surfaces have been observed with the scanning electron microscope (SEM) in order to investigate the failure origin. This analysis has confirmed that all the fatigue failures originated from manufacturing defects. In the following, the defect originating the fatigue failure is called “critical defect.”

First, the fracture surface morphology has been investigated. Two types of morphology have been found. Figure 8A shows a typical fracture surface of failures originating from defects, whereas Figure 8B shows a fish-eye morphology, typical of failures in the VHCF regime. Fish-eye morphology has been found for specimens which failed above  $5 \cdot 10^7$  cycles, two for hourglass specimens and one for notch specimens. Therefore, the fracture surface morphology changes, depending on the number of cycles to failure, with fish-eye failures more likely to occur in the VHCF regime.

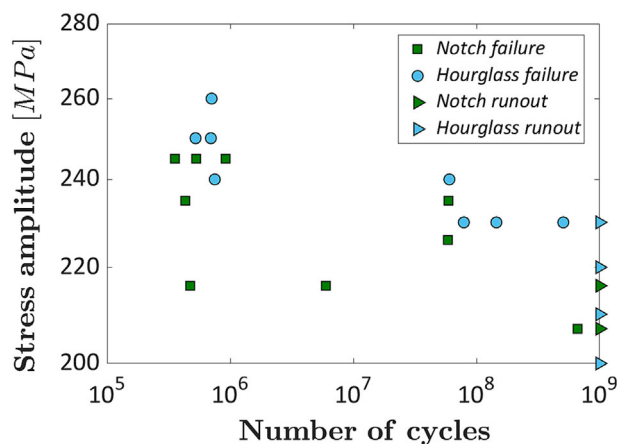


FIGURE 7 S–N plot of the experimental data. [Colour figure can be viewed at [wileyonlinelibrary.com](https://onlinelibrary.wiley.com/terms-and-conditions)]

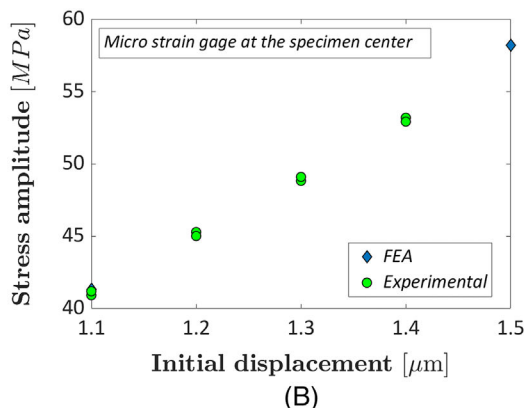
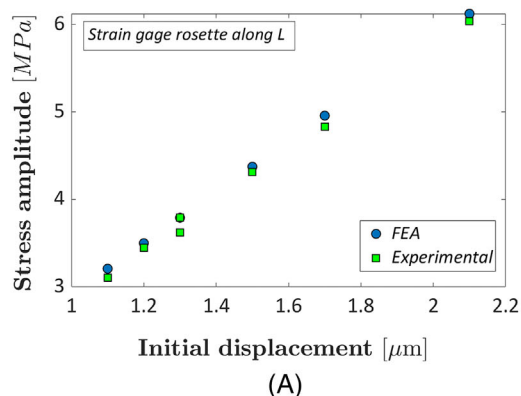


FIGURE 6 Stress amplitude with respect to the displacement exerted by the piezoelectric transducer: (A) calibration with strain gage 1 and (B) calibration with strain gage 2. [Colour figure can be viewed at [wileyonlinelibrary.com](https://onlinelibrary.wiley.com/terms-and-conditions)]

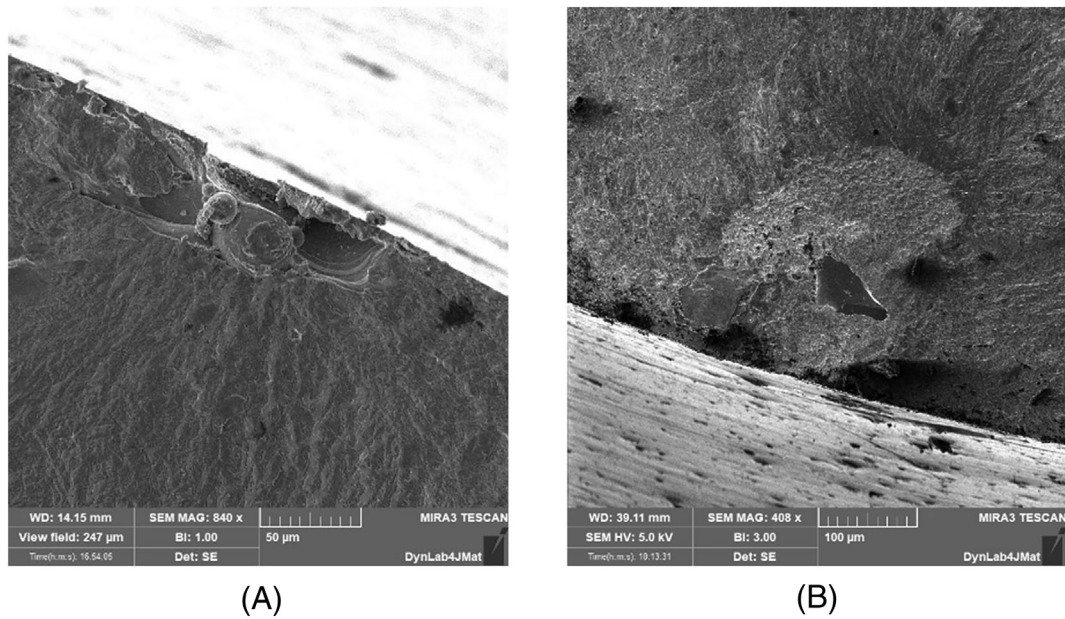


FIGURE 8 Fracture surface morphology: (A) failure from defect and (B) failure from defects with fish-eye morphology.

Critical defects are those generally found in AM specimens, like lack of fusion defects or large surface defects, shown in Figure 9. All critical defects are concentrated close or in touch with the specimen surface, with the largest distance from the specimen surface equal to 250  $\mu\text{m}$ . Thus, regardless of the tested specimens, surface defects have been found to be the most detrimental. This can be explained by considering that the specimens have been tested in the as-built like condition, subject only to a manual polishing and without further posttreatments, like machining. Accordingly, an outer thin layer of material has been removed and large defects close to the surface layer have not been removed or eliminated.

The defect size, the factor that mostly affects the fatigue response,<sup>7</sup> has been then investigated. The square root of the area of the defect in a direction perpendicular to the first principal stress,  $\sqrt{a_c}$ , has been considered as the characteristic defect size.<sup>7,30</sup>  $\sqrt{a_c}$  has been assumed to follow a largest extreme value distribution (LEVD), according to the literature.<sup>7, 30</sup> Figure 10 shows the Gumbel plot of the defect size. For defects showing an irregular morphology, an equivalent size has been considered according to the rules provided in Masuo et al.<sup>30</sup> and based on the fracture mechanics approach. The equivalent defect size allows to reliably compare defects with different origins and morphologies. In Figure 10, the estimated LEVD functions are also shown.

According to Figure 10, defects in hourglass specimens are larger than defects in notched specimens. The largest defect in unnotched specimens is equal to 261  $\mu\text{m}$ , whereas the largest defect in notched specimens is equal

to 177  $\mu\text{m}$  (47% difference). Moreover, all defects in notched specimens are smaller than 177  $\mu\text{m}$ , whereas six out of eight (about 75%) defects in unnotched specimens are above 200  $\mu\text{m}$ . In unnotched specimens, two small defects with sizes close to 100  $\mu\text{m}$ , about half of the other  $\sqrt{a_c}$ , have been found. These small defects originated a fish-eye morphology. Similarly, the smallest defect found in notch specimens ( $\sqrt{a_c} = 54 \mu\text{m}$ ) is the only one originating a fatigue failure with fish-eye morphology, with a fatigue life above  $5 \cdot 10^8$  cycles. In both specimen types, the size of defects originating a fish-eye morphology is significantly smaller than the size of other defects and, in general, below 100  $\mu\text{m}$ . This confirms that a fish-eye morphology, typical of VHCF failures, is more likely to occur as  $\sqrt{a_c}$  decreases, with significantly long fatigue lives.<sup>31</sup>

The reason for the larger defects in hourglass specimens has been moreover investigated and attributed to the different risk volumes of the tested specimens. According to Murakami,<sup>7</sup> the risk volume, or  $V_{90}$ , has been assumed as the volume of material subjected to a stress amplitude above the 90% of the maximum applied stress. This parameter provides an idea of the volume of material at risk of crack nucleation. The  $V_{90}$  of unnotched specimens is equal to 290  $\text{mm}^3$ , whereas the  $V_{90}$  of notched specimens is one order of magnitude less, equal to 15  $\text{mm}^3$ . Manufacturing defects randomly originate during the layer-by-layer process and failure originates if a defect with critical size randomly forms where the stress amplitude is high. According to Murakami,<sup>7</sup> the probability of large and critical defects increases with the risk volume, that is, larger defects are more likely to



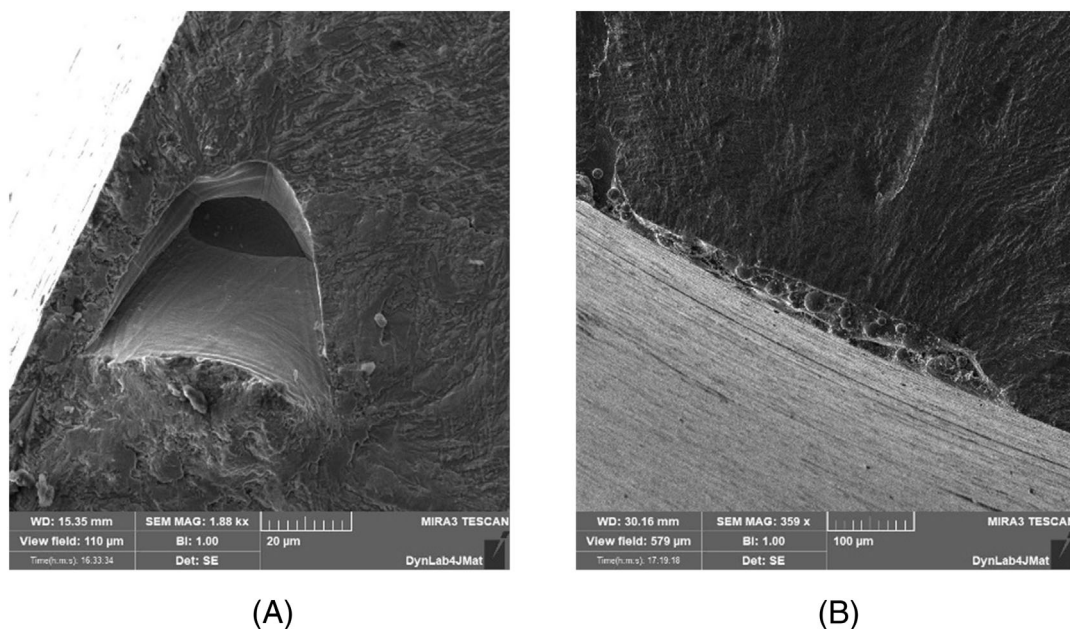


**FIGURE 9** Defects at the origin of the fatigue failures in notched and hourglass specimens: (A) lack of fusion defect and (B) large surface defect.

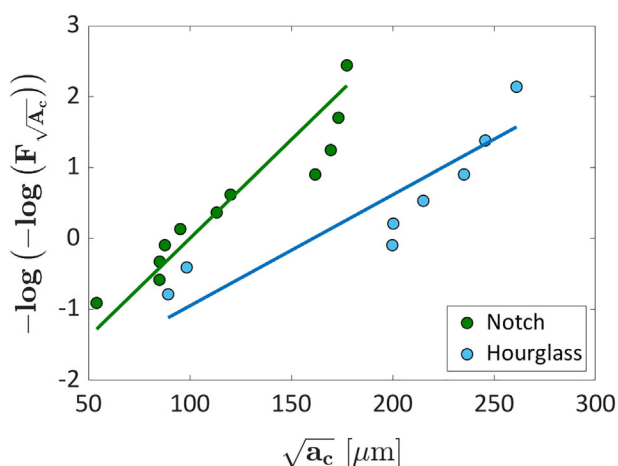


**FIGURE 10** Gumbel plot of the defect size found on the fracture surfaces of notched and unnotched specimens. [Colour figure can be viewed at [wileyonlinelibrary.com](http://wileyonlinelibrary.com)]

occur in large risk volumes (size effect). The probability of large and critical defects in the small volume with high-stress concentration close to the notch tip is therefore small, and as expected, critical defects in notch specimens have been found to be smaller. These small defects, not critical in hourglass unnotched specimens, have in any case originated the fatigue failure in notched specimens, since subjected to the high stress induced by the notch. This explains why, even if  $\sqrt{a_c}$  are significantly different between the two investigated specimens, the difference between the fatigue response in the S–N plot has been

found to be limited. In particular, according to Figure 7, unnotched specimens are characterized by a larger fatigue strength in the LCF–HCF region (below  $10^6$  cycles) where the influence of the peak stress is dominant, whereas the difference tends to reduce in the VHCF region, where defect size plays the most significant role.<sup>32,33</sup>

In order to verify that the defect size plays the major role in the failure origin of the investigated specimens, Figure 11 plots the stress intensity factor ( $K_d$  or SIF), associated to each critical defect, with respect to the equivalent defect size.

According to Figure 11, the experimental data of notched and unnotched specimens follow the same linear trend, in agreement with literature results.<sup>7,30,34</sup> The SIF of hourglass specimens is larger, due to the larger defect size, since the specimens were tested at similar stress amplitudes. This analysis confirms that in both specimens, defect size plays the most significant role and that the failure origin is driven by the random occurrence of a large and critical defect in the material volume with large stress amplitude.

### 3.4 | P–S–N curves and literature results analysis

According to the analyses carried out in Section 3.3, the VHCF failure in the investigated Ti6Al4V alloy is driven by defects, randomly distributed within the risk volume, and by their interactions with the stress gradient within

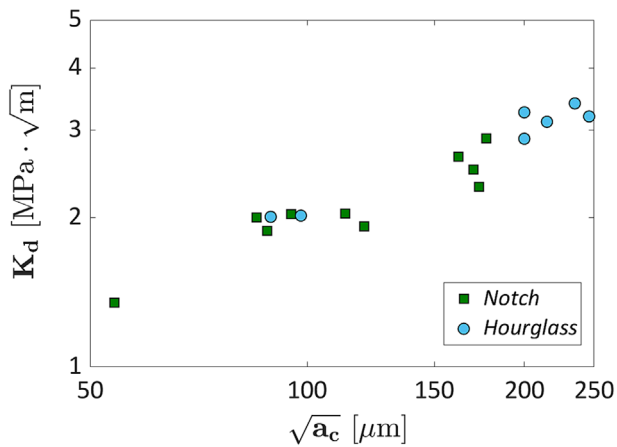


FIGURE 11 Stress intensity factor with respect to the defect size,  $\sqrt{a_c}$ . [Colour figure can be viewed at [wileyonlinelibrary.com](https://onlinelibrary.wiley.com/doi/10.1111/ffe.14078)]

the specimen. To assess the significance of these two factors, that is, defects and the related size effect and the stress gradient, the experimental data have been analyzed with the model proposed in Paolino.<sup>35</sup> In Paolino,<sup>35</sup> size effect is modeled by taking into account the stress gradient and the stress amplitude distribution within the material volume and the defect size distribution. The local stress amplitude  $s_{local}$ , that is, the stress amplitude at the defect location, is considered to assess to real stress involved in the crack formation, computed through FEA starting from the defect location measured with a digital caliber (0.01 mm resolution, in the axial direction) and, in the radial direction, by analyzing the fracture surface images. The model in Paolino,<sup>35</sup> validated on several datasets investigating size effect in VHCF, is based on the weakest link principle, with the fatigue life statistical distribution assumed to follow a Weibull distribution.

Figure 12 plots  $s_{local}$  with respect to the number of cycles to failure. The estimated median, 10th, and 90th quantile P–S–N curves are plotted for the hourglass and notch specimens.

According to Figure 12, the experimental data obtained by testing the hourglass and the notch specimens do not collapse into a unique curve, as expected by considering the local stress amplitude at the defect location. On the other hand, the P–S–N curves for the hourglass specimens are unexpectedly below the corresponding P–S–N curves for notched specimens. This means that the size effect, or better, the effect related to the probabilistic increment of  $\sqrt{a_c}$  with the risk volume, has a dominant effect and counterbalances the stress concentration effect. The experimental scatter is large even by considering the local stress amplitude, highlighting

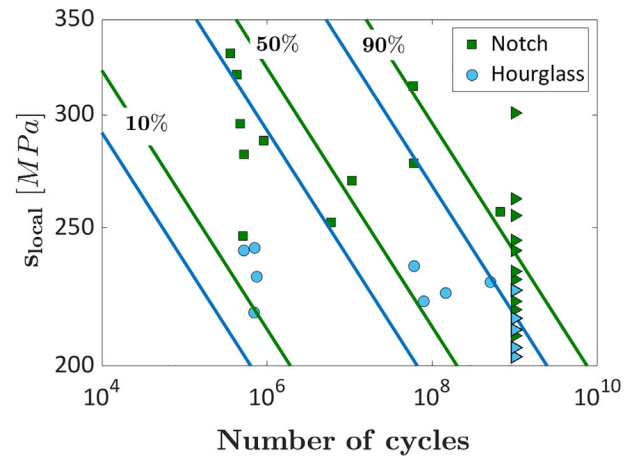


FIGURE 12 S–N plot obtained by considering the local stress amplitude and P–S–N curves estimated with the model in Paolino.<sup>35</sup> [Colour figure can be viewed at [wileyonlinelibrary.com](https://onlinelibrary.wiley.com/doi/10.1111/ffe.14078)]

the significant influence of the randomness associated to the defect size on the VHCF response. To conclude, for the investigated specimens with blunt notches inducing a local peak stress in a small material volume and as-built like surfaces, notch effect has a limited influence, with defects having a prevalent effect. Accordingly, notch effect on the VHCF response of AM specimens must be analyzed by considering not only the stress concentration at the notch tip but also defects and related risk-volume effects, as for HCF test results.<sup>11</sup> To isolate notch effect, experimental tests should be carried out on specimens with the same geometry and risk volume, but this can be rather difficult in ultrasonic fatigue tests, according to Section 2.

Finally, the experimental results obtained in the present paper have been compared with literature results obtained by testing specimens produced with similar process parameters and, above all, subjected to heat treatments with similar properties. In Günther et al.,<sup>24</sup> Ti6Al4V specimens obtained through a machining process of bars manufactured with the SLM process have been tested. The specimens were moreover heat treated with a maximum temperature close to that considered in the present work. A second batch of specimens subjected to hot isostatic pressing (HIP) process after the machining process has been tested. Figure 13 plots the experimental results obtained in the present paper and in Günther et al.<sup>24</sup> in an S–N plot. In Figure 13, “Machining” refers to the specimens subjected to the machining process, whereas “Machined + Hipped” refers to specimens subjected to the HIP process after the machining process in Günther et al.<sup>24</sup> The experimental data in Günther et al.<sup>24</sup> have been digitized from the S–N plot reported in the original paper.

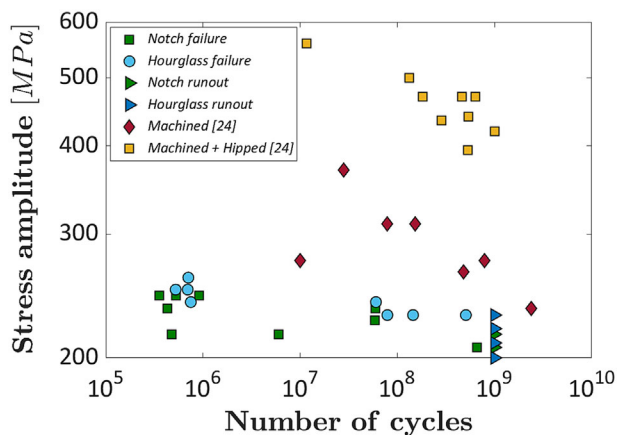


FIGURE 13 S–N plot of the experimental data obtained in the present paper and in Günther et al.<sup>24</sup> [Colour figure can be viewed at [wileyonlinelibrary.com](http://wileyonlinelibrary.com)]

According to Figure 13, the fatigue data obtained in the present paper are below the literature data in Günther et al.<sup>24</sup> The fatigue data of machined specimens are above the fatigue data for the unnotched hourglass specimens, with large differences, proving the significant influence of surface defects and as-built like surface on the VHCF response. The difference increases significantly by considering the literature results obtained by testing specimens subjected to machining and HIP process, which allows closing also internal defects and with crack nucleation shifting to small microstructural defects. This analysis on literature data has further proven the influence of defects and surface quality on the VHCF response of the investigated Ti6Al4V specimens.

## 4 | CONCLUSIONS

In this work, blunt notch effect on the very high cycle fatigue (VHCF) response of Ti6Al4V alloy specimens produced through the selective laser melting (SLM) process is investigated. Fully reversed tension–compression tests have been carried out on hourglass specimens with a blunt notch and without notch, up to  $10^9$  cycles. The following conclusions can be drawn:

1. Specimens with blunt notches have been designed through finite element analyses (FEAs) and by comparing the dynamic stress concentration factor of different specimen shapes commonly tested with ultrasonic fatigue testing machines. The hourglass shape has been found to be the most appropriate geometry, ensuring the required stress concentration and being the easiest to be designed and manufactured.

2. Hourglass specimens with blunt notch (notch specimen in the following, dynamic stress concentration factor equal to 1.42) and hourglass specimens without notches (unnotched specimen in the following, dynamic stress concentration factor equal to 1.02) have been tested. Despite the large experimental variability, the fatigue response of hourglass specimens has been found to be larger than that of notched specimens, but with limited differences, with the data overlapping for number of cycles above  $10^7$  cycles.
3. All the fatigue failures originated from manufacturing defects concentrated close to the surface. In general, fish-eye morphology has been found when defects at the origin of the fatigue failures are smaller than  $100\ \mu\text{m}$  and for fatigue lives above  $10^7$  cycles. Defects in hourglass specimens have been found to be significantly larger, and this was attributed to the different risk volume of the tested specimens, being equal to  $15\ \text{mm}^3$  for the notched specimens and to  $290\ \text{mm}^3$  for the unnotched specimens. Indeed, critical defects are more likely to occur in unnotched specimens with larger risk volumes than in notch specimens (size effect associated to the defect size).
4. Blunt notch has been found to negligibly affect the VHCF response of the investigated SLM Ti6Al4V specimens. Indeed, defects and related size effect limit the stress concentration effect and the “risk volume” has a dominant influence. Notch effect, accordingly, can be counterbalanced by “risk-volume” effect when the fatigue response is driven by defects.

To conclude, the VHCF response of blunt notches SLM specimens with as-built like surfaces, thus with defects mainly concentrated close to the surface, must be analyzed by taking into account the interactions between the defect size distribution, related size effect, and stress amplitude distribution within the part.

## DATA AVAILABILITY STATEMENT


The data that support the findings of this study are available from the corresponding author upon reasonable request.

## ORCID

Andrea Tridello  <https://orcid.org/0000-0003-3007-3377>

Carlo Boursier Niutta  <https://orcid.org/0000-0002-7894-4752>

Filippo Berto  <https://orcid.org/0000-0001-9676-9970>

Davide S. Paolino  <https://orcid.org/0000-0002-4231-4580>

## REFERENCES

1. Khorasani AM, Gibson I, Goldberg M, Littlefair G. A survey on mechanisms and critical parameters on solidification of selective laser melting during fabrication of Ti-6Al-4V prosthetic acetabular cup. *Mater Design*. 2016;103:348-355.
2. Samal SK, Vishwanatha HM, Saxena KK, et al. 3D-printed satellite brackets: materials, manufacturing and applications. *Crystals*. 2022;12(8):1148.
3. Bendsoe MP, Sigmund O. *Topology Optimization: Theory, Methods, and Applications*. Springer; 2004.
4. Sanaei N, Fatemi A, Phan N. Defect characteristics and analysis of their variability in metal L-PBF additive manufacturing. *Mater Design*. 2019;2:108091.
5. Sanaei N, Fatemi A. Defects in additive manufactured metals and their effect on fatigue performance: a state-of-the-art review. *Prog Mater Sci*. 2021;117:100724.
6. Solberg K, Wan D, Berto F. Fatigue assessment of as-built and heat-treated Inconel 718 specimens produced by additive manufacturing including notch effects. *Fatigue Fract Eng Mater Struct*. 2020;43(10):2326-2336.
7. Murakami Y. *Metal Fatigue: Effects of Small Defects and Non-metallic Inclusions*. Elsevier; 2019.
8. Solberg K, Berto F. Notch-defect interaction in additively manufactured Inconel 718. *Int J Fatigue*. 2019;122:35-45.
9. Solberg K, Berto F. A diagram for capturing and predicting failure locations in notch geometries produced by additive manufacturing. *Int J Fatigue*. 2020;134:105428.
10. Molaei R, Fatemi A, Phan N. Notched fatigue of additive manufactured metals under axial and multiaxial loadings, part II: data correlations and life estimations. *Int J Fatigue*. 2022; 156:106648.
11. Emanuelli L, Molinari A, Facchini L, et al. Effect of heat treatment temperature and turning residual stresses on the plain and notch fatigue strength of Ti-6Al-4V additively manufactured via laser powder bed fusion. *Int J Fatigue*. 2022;162:107009.
12. Marines I, Bin X, Bathias C. An understanding of very high cycle fatigue of metals. *Int J Fatigue*. 2003;25:1101-1107.
13. Bathias C, Paris PC. *Gigacycle Fatigue in Mechanical Practice*. 2nd ed. CRC Dekker; 2005.
14. Caivano R, Tridello A, Chiandussi G, Qian G, Paolino DS, Berto F. Very high cycle fatigue (VHCF) response of additively manufactured materials: a review. *Fatigue Fract Eng Mater Struct*. 2021;44(11):2919-2943.
15. Tridello A, Boursier Niutta C, Rossetto M, Berto F, Paolino DS. Statistical models for estimating the fatigue life, the stress-life relation, and the P-S-N curves of metallic materials in very high cycle fatigue: a review. *Fatigue Fract Eng Mater Struct*. 2022;45(2):332-370.
16. Bortoluci Ormastroni LM, Lopez-Galilea I, Pistor J, et al. Very high cycle fatigue durability of an additively manufactured single-crystal Ni-based superalloy. *Addit Manuf*. 2022;54: 102759.
17. Paolino DS, Tridello A, Chiandussi G, Rossetto M. On specimen design for size effect evaluation in ultrasonic gigacycle fatigue testing. *Fatigue Fract Eng Mater Struct*. 2014;37(5): 570-579.
18. Akiniwa Y, Miyamoto N, Tsuru H, Tanaka K. Notch effect on fatigue strength reduction of bearing steel in the very high cycle regime. *Int J Fatigue*. 2006;28(11):1555-1565.
19. Qian G, Hong Y, Zhou C. Investigation of high cycle and very-high-cycle fatigue behaviors for a structural steel with smooth and notched specimens. *Eng Fail Anal*. 2010;17(7-8):1517-1525.
20. Himmelbauer F, Winter G, Grün F, Kiesling C. VHCF properties and assessment of specimens and thin-walled component-like structures made of high-strength steel X5CrNiCuNb16-4. *Int J Fatigue*. 2022;156:106645.
21. Shen J, Fan H, Zhang G, Pan R, Wang J, Huang Z. Influence of the stress gradient at the notch on the critical distance and life prediction in HCF and VHCF. *Int J Fatigue*. 2022;162:107003.
22. Gao Z, Chen X, Zhu S, He Y, Xu W. Notch fatigue behavior of a titanium alloy in the VHCF regime based on a vibration fatigue test. *Int J Fat*. 2023;172:107608.
23. Pilkey WD, Pilkey DF, Zhuming B. *Peterson's Stress Concentration Factors*. John Wiley & Sons; 2020.
24. Günther J, Krewerth D, Lippmann T, et al. Fatigue life of additively manufactured Ti-6Al-4V in the very high cycle fatigue regime. *Int J Fatigue*. 2017;94(2):236-245.
25. Sohar CR, Betzwar-Kotas A, Gierl C, Weiss B, Danninger H. Gigacycle fatigue behavior of a high chromium alloyed cold work tool steel. *Int J Fatigue*. 2008;30(7):1137-1149.
26. Furuya Y, Takeuchi E. Gigacycle fatigue properties of Ti-6Al-4V alloy under tensile mean stress. *Mater Sci Eng A*. 2014;598:135-140.
27. Tridello A, Biffi CA, Fiocchi J, et al. VHCF response of as-built SLM AlSi10Mg specimens with large loaded volume. *Fatigue Fract Eng Mater Struct*. 2018;41(9):1918-1928.
28. ASTM Standard E1876-09. *Standard Test Method for Dynamic Young's Modulus, Shear Modulus, and Poisson's Ratio by Impulse Excitation of Vibration*. ASTM Standard; 2009.
29. Tridello A, Boursier Niutta C, Berto F, Qian G, Paolino DS. Fatigue failures from defects in additive manufactured components: a statistical methodology for the analysis of the experimental results. *Fatigue Fract Eng Mater Struct*. 2021;44(7):1944-1960.
30. Masuo H, Tanaka Y, Morokoshi S, et al. Influence of defects, surface roughness and HIP on the fatigue strength of Ti-6Al-4V manufactured by additive manufacturing. *Int J Fatigue*. 2018; 117:163-179.
31. Tridello A, Fiocchi J, Biffi CA, et al. VHCF response of heat-treated SLM Ti6Al4V Gaussian specimens with large loaded volume. *Procedia Structural Integrity*. 2019;18:314-321.
32. Mughrabi H. On 'multi-stage' fatigue life diagrams and the relevant life-controlling mechanisms in ultrahigh-cycle fatigue. *Fatigue Fract Eng Mater Struct*. 2002;25(8-9):755-764.
33. Mughrabi H. Specific features and mechanisms of fatigue in the ultrahigh-cycle regime. *Int J Fatigue*. 2006;28(11):1501-1508.
34. Meneghetti G, Rigon D, Gennari C. An analysis of defects influence on axial fatigue strength of maraging steel specimens produced by additive manufacturing. *Int J Fatigue*. 2019;118:54-64.
35. Paolino DS. Very high cycle fatigue life and critical defect size: modeling of statistical size effects. *Fatigue Fract Eng Mater Struct*. 2021;44(5):1209-1224.

**How to cite this article:** Tridello A, Boursier Niutta C, Berto F, Paolino DS. Blunt notch effect on the fatigue response up to  $10^9$  cycles of selective laser melting Ti6Al4V specimens. *Fatigue Fract Eng Mater Struct*. 2023;1-12. doi:10.1111/ffe.14078